The Predictive Power of Computational Astrophysics as a Discovery Tool
Proceedings IAU Symposium No. 362, 2023
D. Bisikalo, D. Wiebe & C. Boily, eds.
doi:10.1017/S1743921322001570

Hydrodynamic Simulations and Time-dependent Photoionization Modeling of Starburst-driven Superwinds

A. Danehkar, M. S. Oey and W. J. Gray

Department of Astronomy, University of Michigan, Ann Arbor, MI 48109, USA
email: danehkar@eurekasci.com

Abstract. Thermal energies deposited by OB stellar clusters in starburst galaxies lead to the formation of galactic superwinds. Multi-wavelength observations of starburst-driven superwinds pointed at complex thermal and ionization structures which cannot adequately be explained by simple adiabatic assumptions. In this study, we perform hydrodynamic simulations of a fluid model coupled to radiative cooling functions, and generate time-dependent non-equilibrium photoionization models to predict physical conditions and ionization structures of superwinds using the MAIHEM atomic and cooling package built on the program FLASH. Time-dependent ionization states and physical conditions produced by our simulations are used to calculate the emission lines of superwinds for various parameters, which allow us to explore implications of non-equilibrium ionization for starburst regions with potential radiative cooling.

Keywords. Stars: winds, outflows – galaxies: starburst – hydrodynamics – ISM: bubbles – radiation mechanisms: general – galaxies: star clusters – intergalactic medium

1. Introduction

Thermal and mechanical feedback from OB stars in stellar clusters displaces the surrounding medium in starburst regions on a large scale and forms a galactic-scale outflow named superwind (Heckman et al. 1990), accompanied by a narrow shell and sometime by a hot bubble called superbubble (Weaver et al. 1977). The physical properties of the expanding wind region prior to the bubble and shell have been obtained by Chevalier & Clegg (1985) using adiabatic fluid equations that yield the outflow density $n \propto r^{-2}$ and temperature $T \propto r^{-4/3}$. However, the fluid equations coupled to radiative cooling functions studied by Silich et al. (2004) depict a deviation from the adiabatic temperature, which may explain strong cooling and suppressed superwinds seen in observations of some star-forming galaxies (Oey et al. 2017; Turner et al. 2017; Jaskot et al. 2017). In particular, semi-analytic studies and hydrodynamic simulations demonstrated that radiative cooling is heavily dependent on the metallicity, mass-loss rate, and wind velocity (Silich et al. 2004; Tenorio-Tagle et al. 2005; Gray et al. 2019a; Danehkar et al. 2021). In the case of starburst galaxies where metallicity is low, high mass-loss rates and low outflow velocities contribute to substantial radiative cooling (Danehkar et al. 2021).

Photoionization calculations were performed to identify the superwind models with strong radiative cooling (Gray et al. 2019a; Danehkar et al. 2021). However, emission lines in photoionization (PIE) and collisional ionization equilibrium (CIE) calculated by Danehkar et al. (2021) did not make a clear distinction between those with and without substantial radiative cooling. Previously, photoionization models built with time-dependent non-equilibrium ionization (NEI) states by Gray et al. (2019a) and Gray et al.

(2019b) also indicate that ions such as O VI and C IV could behave differently where plasma is in the NEI case. Non-equilibrium conditions occur when the radiative cooling timescale $\tau_{\rm cool}$ is shorter than the CIE timescale $\tau_{\rm CIE}$ (see e.g. Gnat & Sternberg 2007). In the expanding wind region where plasma is in transition from CIE to PIE at temperatures below 10^6 K, NEI conditions may emerge (Vasiliev 2011) and NEI states could have substantial deviations from CIE states (Gnat & Sternberg 2007; Vasiliev 2011; Oppenheimer & Schaye 2013), which can be identified using the C IV, N V, and O VI lines.

Recently, Danehkar et al. (2021) reported emission line fluxes calculated based on CIE+PIE assumptions using the physical conditions obtained from hydrodynamic simulations with the MAIHEM module in the FLASH program. Similarly, we also computed emission line fluxes following Gray et al. (2019a) for NEI conditions using the time-dependent NEI states and physical properties predicted by our hydrodynamic simulations (Danehkar et al. 2022), showing that the C IV and O VI lines have different behaviors in non-equilibrium photoionized expanding wind regions.

2. Hydrodynamic Simulations

To study starburst-driven superwinds, we consider starburst feedback from a spherically symmetric stellar cluster parameterized by the cluster radius $R_{\rm sc}$, the mass-loss rate $\dot{M}$, and the stellar wind velocity V_∞. The radiation field is characterized by the total stellar luminosity and spectral energy distribution (SED). The surrounding medium has a density $n_{\rm amb}$, while its temperature $T_{\rm amb}$ is dependent on the radiation field and determined by a CLOUDY model.

Our hydrodynamic simulations are performed using the MAIHEM atomic and cooling package (Gray et al. 2015; Gray & Scannapieco 2016; Gray et al. 2019b) in the frame work of the FLASH program (Fryxell et al. 2000), which obtains the solutions for the following one-dimensional spherically symmetric fluid equations coupled to the radiative cooling and photo-heating functions:

$$\frac{d\rho}{dt} + \frac{1}{r^2}\frac{d}{dr}\left(\rho u r^2\right) = q_m, \tag{2.1}$$

$$\frac{d\rho u}{dt} + \rho u \frac{du}{dr} + \frac{dP}{dr} = -q_m u, \tag{2.2}$$

$$\frac{d\rho E}{dt} + \frac{1}{r^2}\frac{d}{dr}\left[\rho u r^2 \left(\frac{u^2}{2} + \frac{\gamma}{\gamma-1}\frac{P}{\rho}\right)\right] = \sum_i n_i \Gamma_i - \sum_i n_i n_e \Lambda_i + q_e, \tag{2.3}$$

where r is the radius, ρ the density, u the velocity, P the thermal pressure, E the total energy per unit mass, $\gamma = 5/3$ the specific heat ratio, $q_m = \dot{M}/(\frac{4}{3}\pi R_{\rm sc}^3)$ and $q_e = (\frac{1}{2}\dot{M}V_\infty^2)/(\frac{4}{3}\pi R_{\rm sc}^3)$ the mass and energy deposition rate per unit volume, respectively, n_i the number densities of ions, n_e the electron number density, Λ_i the radiative cooling rates for a specified temperature from Gnat & Ferland (2012), $\Gamma_i = \int_{\nu_{0,i}}^{\infty}(4\pi J_\nu/h\nu)h(\nu - \nu_{0,i})\sigma_i(\nu){\rm d}\nu$ the photo-heating rates obtained from the given radiation field J_ν and the photoionization cross-section $\sigma_i(\nu)$ (Verner & Yakovlev 1995; Verner et al. 1996), ν the frequency, $\nu_{0,i}$ the ionization frequency, and h the Planck constant.

To set the boundary conditions, we employ the semi-analytic radiative assumptions adopted by Silich et al. 2004, which are based on the adiabatic solutions obtained by Chevalier & Clegg (1985). Accordingly, the density, temperature, and velocity at $r = R_{\rm sc}$ are set to $\rho = \dot{M}/(2\pi R_{\rm sc}^2 V_\infty)$, $T = (\frac{1}{2}V_\infty)^2\mu/(\gamma k_{\rm B})$, and $u = \frac{1}{2}V_\infty$, respectively (μ the mean mass per particle, and $k_{\rm B}$ the Boltzmann constant). For the initial conditions, we set the ambient density specified by an input parameter and the ambient temperature determined by our CLOUDY model, while the medium outside the cluster radius is in stationary states ($u = 0$) at $t = 0$.

https://doi.org/10.1017/S1743921322001570 Published online by Cambridge University Press

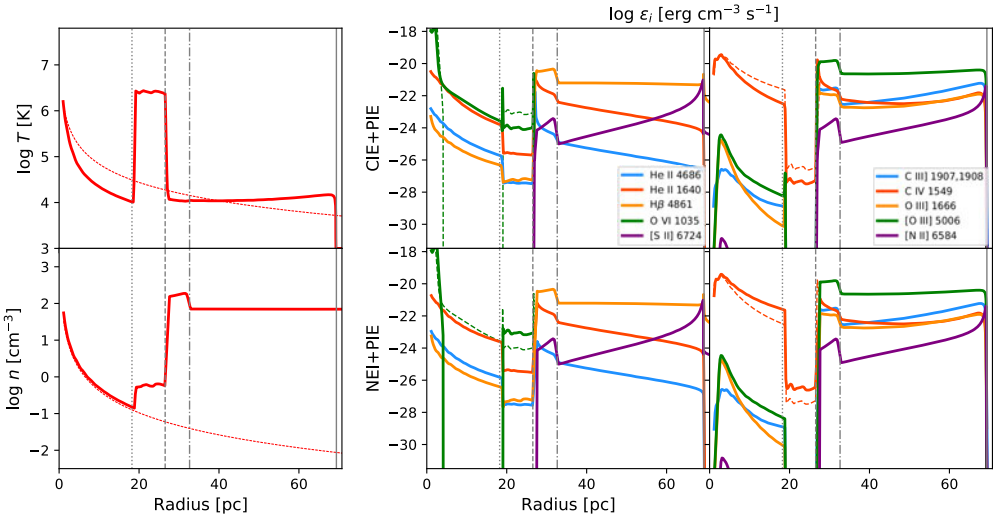

Figure 1. *Left Panels*: The temperature T and density n profiles (solid red lines) predicted by our MAIHEM simulations with the adiabatic solutions (red dashed lines). *Right Panels*: The line emissivities ε_i of the emission lines He II λ4686,λ1640, Hβ λ4861, O VI λ1035, [S II] λ6724 (left), C III] $\lambda\lambda$1907,1908, C IV $\lambda\lambda$1549, O III] λ1666, [O III] λ5006, and [N II] λ6584 (right) calculated by the model in collisional ionization and photoionization equilibrium (CIE+PIE; Danehkar et al. 2021), and in non-equilibrium photoionization (NEI with PIE in the ambient medium; Danehkar et al. 2022). The bubble boundaries, the shell end, and Strömgren sphere are depicted by dotted, dashed, dash-dotted, and solid vertical gray lines, respectively. The wind parameters are: $V_\infty = 457\,\mathrm{km\,s^{-1}}$, $\dot{M} = 0.607 \times 10^{-2}\,\mathrm{M_\odot\,yr^{-1}}$, $t = 1\,\mathrm{Myr}$, the stellar cluster $R_\mathrm{sc} = 1\,\mathrm{pc}$ and $M_\star = 2 \times 10^6\,\mathrm{M_\odot}$, and the medium $n_\mathrm{amb} = 100\,\mathrm{cm^{-3}}$ and $Z/Z_\odot = 0.5$. The O VI and C IV lines predicted by NEI are overplotted by dashed lines in the CIE+PIE panel, and vice versa.

The radiation field J_ν included in our hydrodynamic simulations is generated by the stellar population synthesis program Starburst99 (Levesque et al. 2012; Leitherer et al. 2014) for the rotational stellar models (Ekström et al. 2012; Georgy et al. 2012) with an initial mass function with slope $\alpha = 2.35$ within the range 0.5–150 $\mathrm{M_\odot}$ and the total stellar mass $M_\star = 2 \times 10^6\,\mathrm{M_\odot}$, which are associated with the mass-loss rate $\dot{M} = 10^{-2}\,\mathrm{M_\odot\,yr^{-1}}$ at 1 Myr. The Starburst99 radiation field is applied to the photo-heating rates in MAIHEM to perform non-equilibrium calculations, as well as CLOUDY photoionization models.

Figure 1 (left panels) presents the temperature T and density n radial profiles (solid red lines) generated by our MAIHEM simulation for a model with substantial radiative cooling, along with the expected adiabatic solutions without radiative cooling (dashed lines). The four distinctive regions of a typical superwind defined by Weaver et al. (1977) are also separated by dotted, dashed, and dash-dotted vertical gray color lines, namely expanding wind region (before dotted), bubble (between dotted and dashed), shell (between dashed and dash-dotted), and ambient medium (after dash-dotted vertical lines). The Strömgren sphere (solid vertical gray color line) are determined by a CLOUDY photoionization run on the density profile (pure PIE) following Danehkar et al. (2021).

Figure 2 shows the mean radiative temperature over the mean adiabatic temperature, $f_T \equiv T_\mathrm{wind}/T_\mathrm{adi}$, of the expanding wind region predicted by our MAIHEM hydrodynamic simulations for different wind parameters (V_∞ and $\dot{M}$), ambient densities (n_amb), metallicity ($Z/Z_\odot$), and a stellar cluster with $R_\mathrm{sc} = 1\,\mathrm{pc}$ and $M_\star = 2 \times 10^6\,\mathrm{M_\odot}$, and current age $t = 1$ Myr. The catastrophic cooling (CC) and catastrophic cooling bubble (CB) wind modes, which are with and without bubbles, have $f_T < 0.75$, while the adiabatic bubble (AB) and pressure-confined (AP) mode have $0.75 < f_T < 1.25$. Moreover, the adiabatic

https://doi.org/10.1017/S1743921322001570 Published online by Cambridge University Press

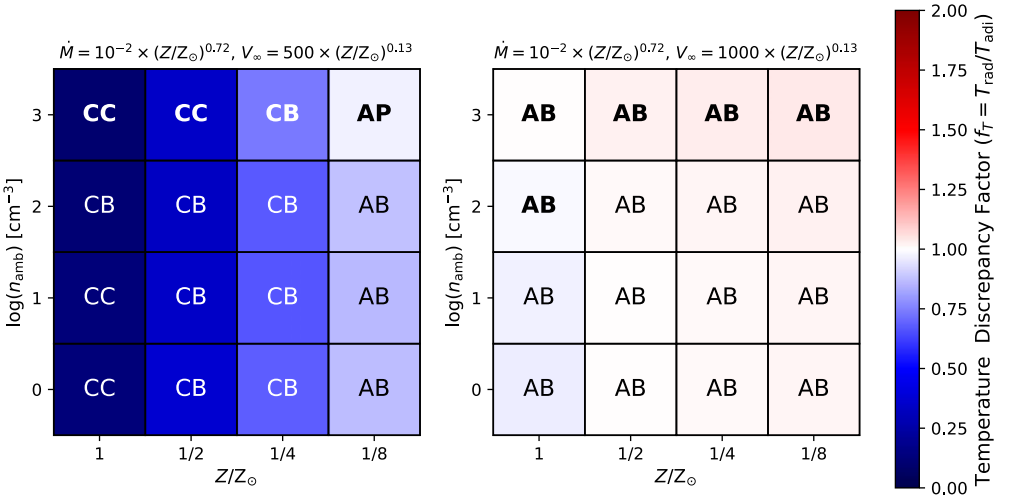

Figure 2. The mean radiative temperature $T_{\rm rad}$ with respect to the mean adiabatic temperature $T_{\rm adi}$ of the expanding wind region for various wind parameters $V_\infty = 500$, and 1000 km s^{-1} and $\dot{M} = 10^{-2} \times (Z/{\rm Z}_\odot)^{0.72}\,{\rm M}_\odot\,{\rm yr}^{-1}$, metallicity $Z/Z_\odot = 0.125$, 0.25, 0.5, and 1, and ambient media with $\log n_{\rm amb} = 0$, 1, 2, and 3 cm^{-3}, surrounding a stellar cluster characterized by $R_{\rm sc} = 1$ pc, $M_\star = 2 \times 10^6\,{\rm M}_\odot$, and age $t = 1$ Myr. The wind models are identified as adiabatic bubble (AB), catastrophic cooling (CC), catastrophic cooling bubble (CB), and pressure-confined (AP), with optically-thick status (bold font), based on criteria defined by Danehkar et al. (2021).

pressure-confined (AP) mode is assigned to those models where the bubble expansion is confined by the ambient thermal pressure (see Danehkar et al. 2021 for more detail). Optically-thick models having neutral ambient medium are also displayed with the bold font. It can be seen that increasing mass-loss rates and decreasing wind velocities result in enhanced radiative cooling in the expanding wind region.

3. Time-dependent Photoionization Models

The physical conditions and NEI states of the expanding wind region made by our hydrodynamic simulations with MAIHEM, along with the radiation field generated by Starburst99, are used to construct non-equilibrium photoionization models with the CLOUDY program (Ferland et al. 2013, 2017). Excluding the NEI states, Danehkar et al. (2021) incorporated the physical properties into a grid of CLOUDY models, which describe the CIE+PIE cases. Inclusion of the NEI states predicted by MAIHEM allows us to emulate non-equilibrium photoionization in the expanding wind region (Danehkar et al. 2022) for which pure PIE is still present in the ambient medium.

In the non-equilibrium conditions, gas kinematic and ionization structures are closely interconnected. The time-dependent NEI states are linked to collisional and dielectronic recombination, collisional ionization, and photoionization rates. The number density of ions n_i for each chemical element in the non-equilibrium cases can be described as

$$\frac{1}{n_{\rm e}}\frac{dn_i}{dt} = n_{i+1}\alpha_{i+1} - n_i\alpha_i + n_{i-1}S_{i-1} - n_iS_i + \frac{1}{n_{\rm e}}n_{i-1}\zeta_{i-1} - \frac{1}{n_{\rm e}}n_i\zeta_i, \qquad (3.1)$$

where α_i includes the radiative recombination rate (Badnell 2006) and dielectronic recombination rates (references given in Table 1 of Gray et al. 2015) for the ionic species i, S_i is the collisional ionization rates (Voronov 1997), $\zeta_i = \int_{\nu_{0,i}}^{\infty}(4\pi J_\nu/h\nu)\sigma_i(\nu){\rm d}\nu$ is the photoionization rates calculated using the specified background radiation field J_ν made by Starburst99 and the photoionization cross-section $\sigma_i(\nu)$.

https://doi.org/10.1017/S1743921322001570 Published online by Cambridge University Press

The non-equilibrium cases appear when the CIE timescale $\tau_{\rm CIE} \approx 1/(n_{\rm e}\alpha_i + n_{\rm e}S_i)$ (Mewe 1999) is longer than the cooling timescale $\tau_{\rm cool} = 3(n_i + n_{\rm e})k_{\rm B}T/(2n_i^2\Lambda_i)$ (Dopita & Sutherland 2003). For less dense environment ($\lesssim 1\,{\rm cm}^{-3}$) that is typical of the expanding wind region, the ions C IV, N V, and O VI satisfy the condition $\tau_{\rm CIE} \geq \tau_{\rm cool}$ at temperatures below 10^6 K, so they could be in the NEI situations in the presence of strong radiative cooling. For $\tau_{\rm CIE} \ll \tau_{\rm cool}$, plasma is in the CIE conditions.

Figure 1 (right panels) presents the emissivities of Hβ, low-excitation [S II] and [N II], and high-excitation He II, [O III], and C III], as well as highly-ionized C IV and O VI calculated by CLOUDY for the physical properties (without the NEI states) produced by our MAIHEM simulation associated with plasma in photoionization and collisional ionization equilibrium (top panel; CIE+PIE), as well as the emissivities computed using CLOUDY following the method of Gray et al. (2019a) for the physical conditions and NEI states generated by our MAIHEM simulation corresponding to the non-equilibrium photoionization situations (bottom panel; NEI with pure PIE in the ambient medium). Large grids for various model parameters are provided as interactive figures by Danehkar et al. (2021) for combined CIE+PIE conditions and Danehkar et al. (2022) for combined NEI+PIE situations, and hosted on this website `https://galacticwinds.github.io/superwinds/`. As seen in Figure 1, the O VI and C IV emissivity profiles in NEI are not the same as those with CIE (see green and orange dashed lines), particularly in the expanding wind region affected by radiative cooling. This behavior can be explained by the time-dependent ionization states of the ions O VI and C IV at temperatures below 10^6 K when rapid cooling faster than ionization processes occurs ($\tau_{\rm cool} < \tau_{\rm CIE}$).

4. Implications for Starburst Galaxies

Our NEI calculations indicate that radiative cooling could enhance the C IV 1550 Å in metal-rich and the O VI 1035 Å doublet in metal-poor environments. The C IV emission line were found in some metal-poor starburst galaxies that are good candidates for suppressed or minimal wind signatures (Senchyna et al. 2017; Berg et al. 2019a,b). As discussed by Gray et al. (2019a), these observations might be associated with kinematic features of suppressed bipolar superwinds rather than resonant scattering mentioned by Berg et al. (2019a). An O VI absorption line associated with a weak outflow was found in Haro 11, while the O VI emission luminosity suggests some cooling loss (Grimes et al. 2007). The O VI λ1035 doublet absorption identified in a gravitationally lensed, galaxy has the features of weak low-ionization winds (Chisholm et al. 2018), which may also be explained by the mass-loss effect under non-equilibrium conditions. Moreover, observations of a star-forming galaxy depict an extended halo in the O VI image, and a weak O VI absorbing outflow in the spectrum (Hayes et al. 2016), which might be an indication of suppressed winds.

The enhancements of the C IV and O VI lines could be related to substantial radiative cooling as suggested by Gray et al. (2019a) and Gray et al. (2019b). Time-dependent NEI states calculated by de Avillez & Breitschwerdt (2012) also imply that O VI can be produced in NEI at $10^{4.2-5}$ K below the temperatures that produce O VI in CIE. Similarly, our NEI calculations (before the shell; see Figure 1) also show that the C IV and O VI emission lines do not behave the same in CIE and NEI, especially in the outflow region strongly impacted by radiative cooling.

Time-dependent ionization processes could also be sensitive to time-evolving ionizing sources. Our radiation field was made by Starburst99 for a typical age of 1 Myr. The radiation field calculated by Starburst99 can evolve with the age, which can affect the formation of radiative cooling in starburst-driven superwinds. Our future hydrodynamic simulations with time-evolving radiation fields will help us to understand better the implication of time-dependent non-equilibrium ionization for star-forming regions.

https://doi.org/10.1017/S1743921322001570 Published online by Cambridge University Press

References

Badnell N. R., 2006, *ApJS*, 167, 334
Berg D. A., Chisholm J., Erb D. K., Pogge R., et al., 2019a, *ApJ*, 878, L3
Berg D. A., Erb D. K., Henry R. B. C., et al., 2019b, *ApJ*, 874, 93
Chevalier R. A., Clegg A. W., 1985, *Nature*, 317, 44
Chisholm J., Bordoloi R., Rigby J. R., Bayliss M., 2018, *MNRAS*, 474, 1688
Danehkar A., Oey M. S., Gray W. J., 2021, *ApJ*, 921, 91
Danehkar A., Oey M. S., Gray W. J., 2022, *ApJ*, 937, 68
de Avillez M. A., Breitschwerdt D., 2012, *ApJ*, 761, L19
Dopita M. A., Sutherland R. S., 2003, Astrophysics of the Diffuse Universe. Springer: Berlin
Ekström S. et al., 2012, *A&A*, 537, A146
Ferland G. J. et al., 2017, *RMxAA*, 53, 385
Ferland G. J. et al., 2013, *RMxAA*, 49, 137
Fryxell B. et al., 2000, *ApJS*, 131, 273
Georgy C., Ekström S., Meynet G., Massey P., et al., 2012, *A&A*, 542, A29
Gnat O., Ferland G. J., 2012, *ApJS*, 199, 20
Gnat O., Sternberg A., 2007, *ApJS*, 168, 213
Gray W. J., Oey M. S., Silich S., Scannapieco E., 2019a, *ApJ*, 887, 161
Gray W. J., Scannapieco E., 2016, *ApJ*, 818, 198
Gray W. J., Scannapieco E., Kasen D., 2015, *ApJ*, 801, 107
Gray W. J., Scannapieco E., Lehnert M. D., 2019b, *ApJ*, 875, 110
Grimes J. P. et al., 2007, *ApJ*, 668, 891
Hayes M., Melinder J., Östlin G., Scarlata C., et al., 2016, *ApJ*, 828, 49
Heckman T. M., Armus L., Miley G. K., 1990, *ApJS*, 74, 833
Jaskot A. E., Oey M. S., Scarlata C., Dowd T., 2017, *ApJ*, 851, L9
Leitherer C., Ekström S., Meynet G., Schaerer D., et al., 2014, *ApJS*, 212, 14
Levesque E. M., Leitherer C., Ekstrom S., Meynet G., Schaerer D., 2012, *ApJ*, 751, 67
Mewe R., 1999, in X-ray spectroscopy in Astrophysics, van Paradijs J., Bleeker J. A., eds., Lectrure Notes in Physics, Springer: Berlin
Oey M. S., Herrera C. N., Silich S., Reiter M., et al., 2017, *ApJ*, 849, L1
Oppenheimer B. D., Schaye J., 2013, *MNRAS*, 434, 1043
Senchyna P. et al., 2017, *MNRAS*, 472, 2608
Silich S., Tenorio-Tagle G., Rodríguez-González A., 2004, *ApJ*, 610, 226
Tenorio-Tagle G., Silich S., Rodríguez-González A., Muñoz-Tuñón C., 2005, *ApJ*, 620, 217
Turner J. L., Consiglio S. M., Beck S. C., Goss W. M., et al., 2017, *ApJ*, 846, 73
Vasiliev E. O., 2011, *MNRAS*, 414, 3145
Verner D. A., Ferland G. J., Korista K. T., Yakovlev D. G., 1996, *ApJ*, 465, 487
Verner D. A., Yakovlev D. G., 1995, *A&AS*, 109, 125
Voronov G. S., 1997, Atom. Data Nucl. Data Tabl., 65, 1
Weaver R., McCray R., Castor J., Shapiro P., Moore R., 1977, *ApJ*, 218, 377